

Investigation of various decay mechanisms for $^{216}\text{Th}^*$ following the $^{32}\text{S} + ^{184}\text{W}$ reaction in the range $E_{\text{c.m.}} = 118\text{--}196$ MeV

Amandeep Kaur* and Manoj K. Sharma

School of Physics and Materials Science, Thapar Institute of Engineering and Technology, Patiala 147004, Punjab, India



(Received 1 November 2018; revised manuscript received 2 March 2019; published 24 April 2019)

Various decay possibilities of the $^{216}\text{Th}^*$ nuclear system formed via interaction of a ^{32}S projectile on a ^{184}W target are investigated within the collective clusterization approach of the dynamical cluster-decay model (DCM). The study is carried out at center-of-mass energies spread across the Coulomb barrier ($118.8 \leq E_{\text{c.m.}} \leq 195.9$ MeV) by including the quadrupole deformations (β_2 static) and optimum orientations ($\theta_i^{\text{opt.}}$) of the decay fragments. According to experimental observation, the noncompound nucleus (nCN) component competes with the compound nucleus (CN) processes [evaporation residue (ER) and fusion-fission (ff)]. The anomalous behavior of calculated fission anisotropies (A) for the $^{216}\text{Th}^*$ nucleus indicates the presence of nCN contributions, such as quasifission (QF) and fast fission (FF). With an aim to have comprehensive analysis of CN and nCN fission mechanisms (ff, QF, FF), the role of center-of-mass energy ($E_{\text{c.m.}}$) and angular momentum (ℓ) is explored in terms of various observables of DCM such as fragmentation potential, preformation probability, scattering potential, and penetrability. The fragmentation potential of the $^{216}\text{Th}^*$ nucleus shows asymmetric fission mass distribution, independent of $E_{\text{c.m.}}$ and ℓ values. The capture excitation functions $\sigma_{\text{cap.}}$ are obtained by adding the DCM-calculated CN ($\sigma_{\text{CN}} = \sigma_{\text{ER}} + \sigma_{\text{ff}}$) and nCN ($\sigma_{\text{nCN}} = \sigma_{\text{QF}} + \sigma_{\text{FF}}$) contributions. The calculated cross sections find nice agreement with the experimental data, and the evaporation residue contribution is predicted to be negligibly small. The compound nucleus fusion/formation probability P_{CN} is estimated as a function of $E_{\text{c.m.}}$, which in turn suggests that the maximum contribution from the CN channel is $\approx 66\%$. Finally, the effect of β_2 -dynamic deformations on the various decay mechanisms of the $^{216}\text{Th}^*$ nucleus is explored at highest center-of-mass energy (195.9 MeV), where nCN processes start competing with the CN decay mechanism.

DOI: [10.1103/PhysRevC.99.044611](https://doi.org/10.1103/PhysRevC.99.044611)

I. INTRODUCTION

The dynamics of reactions involving actinide nuclei have been explored rigorously in recent years. This is attributed to the fact that such reactions play a crucial role in the expansion of the periodic table, synthesis of new elements, and production of isotopes beyond the β -stability line. Persistent theoretical and experimental attempts have been made to investigate various reactions' conditions and their subsequent influence on the decay mechanism [1–5].

In heavy-ion reactions (HIR), the possibility of an equilibrated state of the composite system depends on numerous factors such as the mass asymmetry (α) of the entrance channel with respect to the Businaro-Gallone mass asymmetry parameter (α_{BG}) [6], incident energy with respect to the Coulomb barrier, the charge product $Z_P Z_T$ (where Z_P and Z_T are the proton numbers of projectile and target), deformations, and orientations. If the composite system is fully equilibrated, it involves the complete amalgamation of projectile and target nucleons at the compound nucleus (CN) stage, which may decay via the emission of evaporation residue (ER) and fusion-fission (ff) fragments. In contrast, a nonequilibrated fused nuclear system, i.e., a noncompound nucleus (nCN), reseparates prior to complete amalgamation by transferring

only a few nucleons, thus giving rise to different decay processes such as quasifission (QF), fast fission (FF), etc.

The quasifission (QF) process is observed in reactions involving heavy target projectile combinations, exhibiting large Coulomb repulsion and centrifugal potential. In such reactions, multinucleon transfer takes place and the composite system so formed reseparates into two fragments. The reseparation occurs at relatively faster pace (as compared to formation of an equilibrated CN) and projectilelike fragments are formed in the exit channel. Owing to the relatively small interaction time involved in transfer of nucleons, the decay fragments obtained in QF retain the entrance channel properties. A wider mass distribution and fairly large fission fragment anisotropy are some tested signatures of the QF process. Earlier studies of QF suggest that the deformation and orientation degrees of freedom play a significant role, as the deformed targets with tip-to-tip collision give rise to QF, while the side collisions generally result in the ff process [7].

Partial waves up to maximum angular momentum (ℓ_{max}) contribute to the CN fusion/formation cross sections. ℓ_{max} represents that angular momentum value where light particle cross sections become negligibly small. The CN formation is affected by centrifugal forces. The fission barrier of CN decreases with increasing ℓ values, and disappears at an ℓ value (called ℓ_{Bf}) which is lower than ℓ_{max} [8]. This suggests the possible emergence of another mechanism known as fast fission (FF). FF is a process which is observed

* amanganday@gmail.com

when the potential barrier disappears due to large centrifugal force appearing across higher angular momentum (i.e., $\ell > \ell_{\text{Bf}}$) [9]. FF occurs at a faster pace, with reaction time 10^{-21} – 10^{-20} s, but larger reaction time than deep inelastic collisions (DIC) (10^{-22} – 10^{-21} s), therefore it is also known as delayed DIC [10]. The main difference between the two nCN processes is that FF is observed only above ℓ_{Bf} values whereas QF is operative at lower ℓ states as well.

The identification of the contribution of various competing CN and nCN decay channels is an intricate process. Because either the experimental signatures of these decay channels overlap, thus making it difficult for them to be identified individually, or their contribution is less prominent, hence impeding theoretical evaluation [11]. In general, several experimental tools are available to look for the existence of nCN fission in a nuclear reaction. A brief description of such efforts is outlined below:

- (i) The simple way to observe the existence of nCN content in a reaction is to measure the fission fragment angular anisotropies and compare them with the theoretical calculations [12,13].
- (ii) The separation of two fragments during nCN process takes place in a very short timescale as compared to the CN process [10,14], therefore, the direct evidence of different CN and nCN processes can be observed in terms of reaction times.
- (iii) The fission fragments originating from the nCN process are often characterized by their broad mass distribution, mass angle correlations, kinetic energy and angular distributions, etc. [13,15], which indicate a nonequilibrium origin and short sticking time of the decaying system compared to those originating from CN fission.
- (iv) Recently, γ rays were used as a probe to distinguish between CN and nCN fission on the basis of their angular momenta [16]. However, identification of the reaction mechanism is not always unambiguous using the above mentioned probes.

The main interest of the present work is to explore the individual contribution of competing CN and nCN decay channels in the dynamics of the $^{32}\text{S} + ^{184}\text{W} \rightarrow ^{216}\text{Th}^*$ reaction. For this reaction, the entrance channel mass asymmetry α is 0.703, which is smaller than the Businaro-Gallone mass asymmetry [6], i.e., $\alpha_{\text{BG}} = 0.864$. Thus, according to the preequilibrium fission model [12,17], nCN fission may be present in the decay of the $^{216}\text{Th}^*$ nucleus. Moreover, the nCN component is expected to compete with the CN process at $Z_P Z_T \geq 1000$ [18], due to the large entrance channel Coulomb repulsion. It may be worth noting that the product of $Z_P Z_T$ for the considered reaction is 1184, hence there exists a possibility of hindrance in the CN formation.

In view of this, the dynamical cluster-decay model (DCM) is employed to study the relevant contribution of decay mechanisms for CN (ER and ff) and nCN (QF and FF) processes involved in the dynamics of the $^{32}\text{S} + ^{184}\text{W}$ reaction, in reference to the experimental finding of Zhang *et al.* [19]. Interestingly, the experimental data [19] are available on the

either side of the Coulomb barrier for this reaction, which provides us an opportunity to investigate the dynamics involved with CN and nCN decay below and above barrier energies. Evidently, the DCM has been successfully applied to study different CN and nCN processes for decay in preactinide, actinide, and superheavy mass regions [20–27]. It may be noted that the collective clusterization approach is being employed for the first time to explore the dynamics associated with fast fission mechanism. The characteristics of fragmentation potential, preformation probability P_0 , barrier penetrability P , and scattering potential are analyzed at different incident energies and angular momentum values. In this study, the deformation effects are included up to quadrupole deformations (β_2 static) with optimum orientations (θ_i^{opt}) of the decay fragments. Knowing that the anisotropy (A) is an effective tool to investigate the presence/absence of CN and nCN components, the fission anisotropies are calculated within the standard saddle-point statistical model (SSPSM) [28] using DCM-based parameters. In addition to this, compound nucleus fusion/formation probability P_{CN} is determined as a function of center-of-mass energy $E_{\text{c.m.}}$, to analyze the role of CN and nCN contributions in the total capture cross sections. Also, the possible fragmentation path in reference to temperature-dependent deformations from Refs. [29,30] is worked out to analyze the possible role of β_2 -dynamic deformations in the decay of the $^{216}\text{Th}^*$ nucleus.

The present article is organized as follows: The description of DCM used for decay analysis is given in Sec. II. The calculations and results of different fission mechanisms are discussed in Sec. III, and, finally, the summary and conclusions are presented in Sec. IV. A brief report of this work was presented at the national conference on “Recent Advances in Experimental and Theoretical Physics” (RAETP-2018), held in Jammu, India [31].

II. THE MODEL

Different decay mechanisms of the hot and rotating $^{216}\text{Th}^*$ nuclear system formed via the $^{32}\text{S} + ^{184}\text{W}$ reaction at various center-of-mass energies $E_{\text{c.m.}}$ are analyzed using the dynamical cluster-decay model (DCM). The DCM [20–27] was developed using the well-known quantum mechanical fragmentation theory (QMFT) [32–34], which works in terms of collective coordinates of mass (and charge) asymmetries $\eta_A = (A_1 - A_2)/(A_1 + A_2)$ [and $\eta_Z = (Z_1 - Z_2)/(Z_1 + Z_2)$] (where 1 and 2 stand for heavy and light fragments), relative separation R , the multipole deformations $\beta_{\lambda i}$ ($\lambda = 2, 3, 4$; $i = 1, 2$), and orientations θ_i ($i = 1, 2$). In terms of these coordinates, for ℓ partial waves, the decay and fragment’s production cross section is given by

$$\sigma(A_1, A_2) = \frac{\pi}{k^2} \sum_{\ell=0}^{\ell_{\text{max}}} (2\ell + 1) P_0 P, \quad k = \sqrt{\frac{2\mu E_{\text{c.m.}}}{\hbar^2}}, \quad (1)$$

where $\mu = m[A_1 A_2 / (A_1 + A_2)]$ is the reduced mass. P_0 , the fragment’s preformation probability, refers to η motion at fixed R value; and P , the barrier penetrability, refers to R motion for each η value. Following equation (1), the cross sections of ER and ff processes (i.e., σ_{ER} and σ_{ff}) are calculated

as

$$\sigma_{\text{ER}} = \sum_{A_2=1}^4 \sigma(A_1, A_2), \quad \sigma_{\text{ff}} = 2 \sum_{A_2=A/2-20}^{A/2} \sigma(A_1, A_2), \quad (2)$$

giving the cross section of CN decay $\sigma_{\text{CN}} = \sigma_{\text{ER}} + \sigma_{\text{ff}}$.

The preformation factor P_0 contains structure information of the compound nuclear system, that enters via fragmentation potential $V_R(\eta, T)$ in the Schrödinger equation, defined as

$$\begin{aligned} V_R(\eta, T) = & \sum_{i=1}^2 [V_{\text{LDM}}(A_i, Z_i, T)] + \sum_{i=1}^2 [\delta U_i] \exp(-T^2/T_0^2) \\ & + V_C(R, Z_i, \beta_{\lambda i}, \theta_i, T) + V_P(R, A_i, \beta_{\lambda i}, \theta_i, T) \\ & + V_\ell(R, A_i, \beta_{\lambda i}, \theta_i, T). \end{aligned} \quad (3)$$

Here, V_C , V_P , and V_ℓ are respectively, the T -dependent Coulomb, nuclear proximity, and centrifugal potentials for deformed and oriented nuclei (for details see Ref. [35]). V_{LDM} is the T -dependent liquid drop energy of Davidson *et al.* [36] and δU the ‘‘empirical’’ shell correction, as stated in Ref. [37], made T dependent as per [38]. The constants of V_{LDM} at $T = 0$ are refitted [35,39,40] to give the experimental binding energies of Audi *et al.* [41] or the theoretical estimates of Möller *et al.* [42] wherever not available in Ref. [41]. The static deformations of nuclei are taken up to quadrupole deformations β_{2i} from the theoretical estimates of Möller and Nix [42], and the orientations are the ‘‘optimum’’ orientations θ_i^{opt} for ‘‘hot-compact’’ configuration [43]. The deformation parameter β_{2i} is also taken to be temperature dependent [29,30], by using the relation $\beta_{\lambda i}(T) = \exp(-T/T_0)\beta_{\lambda i}(0)$, where $\beta_{\lambda i}(0)$ is the static deformation and T_0 is the temperature of the nucleus at which shell effects start to vanish ($T_0 = 1.5$ MeV) [38].

The rotational energy V_ℓ is given as

$$V_\ell(R, A_i, \beta_{\lambda i}, \theta_i, T) = \frac{\hbar^2 \ell(\ell + 1)}{2I(T)}, \quad (4)$$

with $I = I_S = \mu R^2 + \frac{2}{5}A_1 m R_1^2(\alpha_1, T) + \frac{2}{5}A_2 m R_2^2(\alpha_2, T)$, the moment of inertia in the sticking limit, which for the non-sticking limit reads as $I = I_{\text{NS}} = \mu R^2$.

The preformation probability P_0 is obtained using the fragmentation potential $V_R(\eta, T)$ by solving the Schrödinger equation in η coordinates at fixed $R = R_a$,

$$\left\{ -\frac{\hbar^2}{2\sqrt{B_{\eta\eta}}} \frac{\partial}{\partial \eta} \frac{1}{\sqrt{B_{\eta\eta}}} \frac{\partial}{\partial \eta} + V(\eta, R, T) \right\} \psi^\nu(\eta) = E^\nu \psi^\nu(\eta), \quad (5)$$

with $\nu = 0, 1, 2, 3, \dots$ referring to ground state ($\nu = 0$) and excited state solutions, with the ground state P_0 given as

$$P_0 = |\psi(\eta(A_i))|^2 \sqrt{B_{\eta\eta}} \frac{2}{A_{\text{CN}}}, \quad (6)$$

and with the Boltzmann-like function

$$|\psi|^2 = \sum_{\nu=0}^{\infty} |\psi^\nu|^2 \exp(-E^\nu/T). \quad (7)$$

$B_{\eta\eta}$ in Eq. (6) represents the smooth hydrodynamical mass parameter [44]. It may be noted that in DCM based calculations,

for the QF decay channel, the preformation probability is taken as unity, i.e., $P_0 = 1$. This is because the QF corresponds to an intermediate nonequilibrated nCN process, where the incoming channel is supposed to retain its identity [45].

The penetration probability P in Eq. (1) is the Wentzel-Kramers-Brillouin (WKB) integral,

$$P = \exp \left[-\frac{2}{\hbar} \int_{R_a}^{R_b} \{2\mu[V(R) - Q_{\text{eff}}]\}^{1/2} dR \right] \quad (8)$$

with $V(R_a, T) = V(R_b, T) = \text{TKE}(T) = Q_{\text{eff}}(T)$ for the two turning points.

In the case of fast fission, the fission barrier becomes vanishingly small at higher angular momentum values ($\ell > \ell_{\text{Bf}}$), which indicates maximum penetration probability for the contributing fission fragments ($P \approx 1$). The first turning point of the penetration path, R_a , is defined as

$$\begin{aligned} R_a(T) &= R_1(\alpha_1, T) + R_2(\alpha_2, T) + \Delta R(T) \\ &= R_i(\alpha, T) + \Delta R(T), \end{aligned} \quad (9)$$

with radius vectors R_i ($i = 1, 2$),

$$R_i(\alpha_i, T) = R_{0i}(T) \left[1 + \sum_{\lambda} \beta_{\lambda i} Y_{\lambda}^{(0)}(\alpha_i) \right], \quad (10)$$

and T -dependent nuclear radii R_{0i} of the equivalent spherical nuclei [46],

$$R_{0i}(T) = [1.28A_i^{\frac{1}{3}} - 0.76 + 0.8A_i^{\frac{-1}{3}}] (1 + 0.0007T^2) \text{ fm}. \quad (11)$$

ΔR is the only parameter of the model, and is known as the neck-length parameter. The nuclear temperature (T) is related to compound nucleus excitation energy as $E_{\text{CN}}^* = E_{\text{c.m.}} + Q_{\text{in}} = (A_{\text{CN}}/9)T^2 - T$.

Finally, the fission fragment anisotropy (A) calculated within the standard saddle-point statistical model (SSPSM) [28] is given by

$$A = 1 + \langle \ell^2 \rangle / 4K_0^2, \quad (12)$$

where $\langle \ell^2 \rangle$ is the mean square angular momentum of fissioning nucleus related to the total ℓ value (equivalently, ℓ_{max} of the CN). The value of ℓ_{max} depends on the sticking limit (I_S) and nonsticking limit (I_{NS}) in the centrifugal potential. Note that I_{NS} is preferred [25,47,48] for fission anisotropy calculations. K_0^2 is the variance of the K distribution related to the effective moment of inertia I_{eff} of the CN, given as

$$K_0^2 = T \times I_{\text{eff}} / \hbar^2. \quad (13)$$

I_{eff} is calculated by using the finite-range rotating liquid drop model [49], with T being the temperature of fissioning nucleus.

III. CALCULATIONS AND DISCUSSION

This section presents the calculations for various decay processes of $^{216}\text{Th}^*$ formed in the $^{32}\text{S} + ^{184}\text{W}$ reaction over a wide range of center-of-mass energies around the Coulomb barrier, $E_{\text{c.m.}} = 118.8$ to 195.9 MeV. First, in Sec. III A, the CN (ff) and nCN (QF and FF) fission contributions are

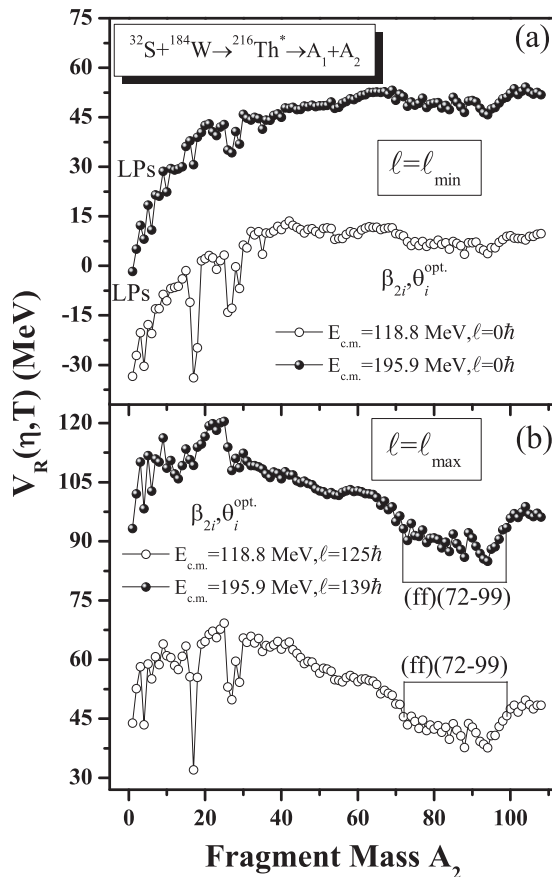


FIG. 1. Mass fragmentation potential for the nuclear system $^{216}\text{Th}^*$ formed in $^{32}\text{S} + ^{184}\text{W}$ reaction at extreme energies $E_{\text{c.m.}} = 118.8$ and 195.9 MeV, using the best fitted ΔR 's, plotted for (a) minimum (ℓ_{min}) and (b) maximum (ℓ_{max}) values of angular momentum.

explored within the framework of DCM. The deformation effects are included up to static quadrupole deformation (β_2 static) using optimum orientation criteria θ_i^{opt} [43]. For heavy-ion reactions, the fission fragment anisotropy (A) is an unambiguous tool to investigate nCN fission, and the same is explored here within the SSPSM approach in reference to the data of Ref. [19]. The detailed analysis of potential energy surfaces (PES), preformation factor P_0 , penetrability P , and scattering potential $V(R)$ effects is carried out to investigate different fission mechanisms (ff, QF, and FF). For a comprehensive analysis of CN and nCN processes, the compound nucleus fusion probability P_{CN} is calculated over a wide range of incident energies. Further, Sec. III B presents the possible role of temperature-dependent deformations (β_2 dynamic) on the various decay mechanisms of the $^{216}\text{Th}^*$ nucleus.

A. CN and nCN fission of the $^{216}\text{Th}^*$ nucleus at energies across the Coulomb barrier

Figure 1(a) depicts the fragmentation potential $V_R(\eta, T)$ for the decay of the $^{216}\text{Th}^*$ nucleus at two extreme center-of-mass energies, $E_{\text{c.m.}} = 118.8$ and 195.9 MeV, at minimum (ℓ_{min}) angular momentum, while Fig. 1(b) depicts the behavior at maximum (ℓ_{max}) angular momentum. The calculated T -dependent collective potential energy $V_R(\eta, T)$ gives

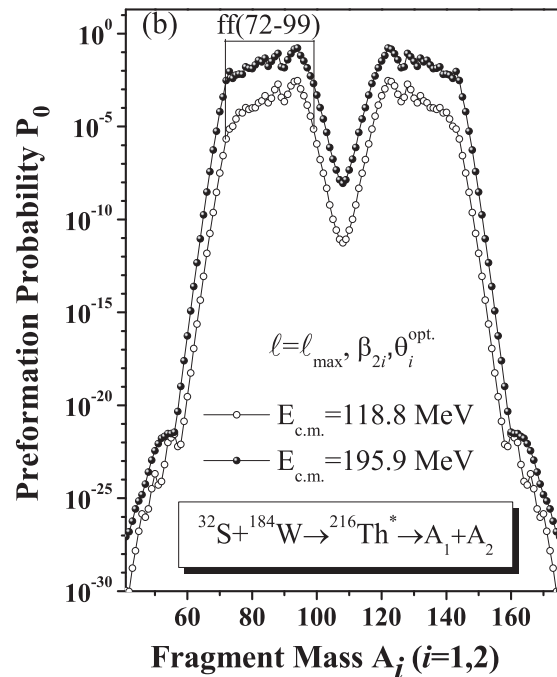


FIG. 2. The preformation probability P_0 for the decay of an excited $^{216}\text{Th}^*$ nucleus as a function of fragment mass A_i ($i = 1, 2$) at two extreme center-of-mass energies, $E_{\text{c.m.}} = 118.8$ and 195.9 MeV, for ℓ_{max} states.

the relative contribution of possible decay fragments. It is noticed from the figure that lower ℓ states are energetically more favorable for light particles (LPs) and higher ones for the fission fragments (ff). The magnitude of fragmentation potential increases with increase in energy and angular momentum. At extreme energies, the structure of the fragmentation potential for evaporation residues ($A_2 \leq 4$) and intermediate mass fragments (IMFs) is different, whereas the structure of fission region remains almost same. Further, at higher angular momentum, for extreme energies, the fission region depicts a potential energy minimum (equivalently, the maximum in preformation probability P_0 ; see Fig. 2). This confirms that the fission component dominates at large ℓ value. Moreover, at both extreme $E_{\text{c.m.}}$, the minimum in fragmentation potential corresponds to the same fragment mass range, i.e., $A_2 = 72-99$ (plus complementary fragments). The variation of the potential energy surface reveals that $^{216}\text{Th}^*$ shows an asymmetric mass distribution, which is in line with the observation drawn from the $^{233}\text{Th}^*$ nucleus formed in the neutron induced reaction $n + ^{232}\text{Th} \rightarrow ^{233}\text{Th}^*$ [50]. This suggests that the potential energy surface(s) for the Th nucleus is independent of the incident projectile and energy. It is relevant to mention that, in the framework of DCM, the preformation factor P_0 is the solution of the stationary Schrödinger equation in η coordinate, where the fragmentation potential [see Eq. (3) and Fig. 1] goes as input.

After studying the variation of the fragmentation potential, we analyze the dynamics of the $^{32}\text{S} + ^{184}\text{W}$ reaction through the preformation probability P_0 (see Fig. 2), plotted as a function of heavy mass fragments at ℓ_{max} , as the fission contribution becomes prominent at higher ℓ values. Comparing the

TABLE I. The SSPSM/DCM calculated fission anisotropies A using nonsticking limit I_{NS} for the moment of inertia for the $^{32}\text{S} + ^{184}\text{W}$ reaction at various $E_{c.m.}$ and compared with experimental anisotropies [19]. Also shown are the anisotropy-fitted neck-length parameter ΔR and other relevant quantities.

$E_{c.m.}$ (MeV)	E_{CN}^* (MeV)	T (MeV)	ℓ_{max} (\hbar)	ΔR (fm)	Anisotropy (A)	
					Calc.	Expt.
118.8	37.2	1.266	16	0.726	1.50	1.51
123.1	41.5	1.336	25	1.070	2.10	2.16
127.3	45.8	1.402	27	1.130	2.22	2.27
131.5	50.0	1.464	33	1.250	2.67	2.74
135.8	54.3	1.525	34	1.260	2.68	3.06
141.1	58.5	1.582	35	1.270	2.71	3.28
144.4	61.8	1.626	36	1.300	2.74	3.80

preformation profile at extreme energies, it is observed that the magnitude of P_0 changes while the mass distribution for fission fragments is almost identical and asymmetric in nature, independent of $E_{c.m.}$.

As stated above, the anisotropy of fission products serves as an effective probe to explore the CN and nCN contributions in heavy-ion induced reactions. Henceforth, in the present work, the fission fragment anisotropies (A) of the $^{32}\text{S} + ^{184}\text{W}$ reaction are calculated within the standard saddle-point statistical model (SSPSM) [28] using DCM-based parameters for the nonsticking (I_{NS}) limit of moment of inertia [25]. It is worth noting that, in DCM based calculations, the decay cross sections are estimated using the sticking limit of moment of inertia (I_S), in which the rotation of two touching spheres is considered around their common center of mass. The choice of moment of inertia in the sticking limit is attributed to the use of the proximity potential of Blocki *et al.* [51]. On the other hand, for the fission fragment anisotropies A , it has been observed that the nonsticking limit (I_{NS}) is favored where no intrinsic rotation of fragments is considered due to the small separation distance between them [47,48]. Note the use of the nonsticking limit, generally used in the experimental determination of the ℓ value. Table I presents the calculated and experimental fission anisotropies for the $^{216}\text{Th}^*$ nucleus at different incident energies. The effective moment of inertia I_{eff} in Eq. (13) at the saddle point is calculated using the finite range rotating liquid drop model [49]. It is observed that the calculated anisotropies match with the experimental anisotropies, except at higher excitation energies above the Coulomb barrier (≈ 136 MeV). The deficiency in anisotropy at higher energies indicates the presence of some competing nCN mechanisms, such as quasifission and fast fission. In the framework of SSPSM, it is assumed that the fission fragments are emitted along the symmetry axis of the fissioning nucleus and the K component of the total angular momentum along the symmetry axis is conserved during the descent from saddle to scission point [52]. For the case of heavy systems, this assumption may not be justified where the saddle and scission point configurations have very different shapes. Therefore, in the present case, the SSPSM may not properly describe the fission anisotropies in reactions with massive nuclei at higher energies. Hence, it may be concluded that the anomalous

behavior of fission anisotropies indicates the presence of nCN content in the decay of the $^{216}\text{Th}^*$ nucleus, especially at above-barrier energies.

In addition to this, as discussed in the Sec. I, the mass asymmetry [$\alpha = (A_T - A_P)/(A_T + A_P)$] of interacting nuclei and the product $Z_P Z_T$ play significant roles in determining the contributions from the nCN fission processes. It is evident from the literature [53] that if $\alpha < \alpha_{BG}$ then there is a possibility of nCN contributions. In fact, the Businaro-Gallone mass asymmetry α_{BG} is a parameter which separates the mass symmetric liquid drop fission barrier from the asymmetric one [6]. For the $\alpha > \alpha_{BG}$ case, the mass flows from projectile to target nucleus and results in an equilibrated composite system (i.e., CN), whereas for $\alpha < \alpha_{BG}$ the mass flows in the direction of the dinuclear system, which decays before achieving equilibrium, thus giving rise to the nCN process [53]. For the considered reaction channel $^{32}\text{S} + ^{184}\text{W}$, $\alpha (=0.703) < \alpha_{BG} (=0.864)$ which indicates the presence of the nCN contribution from this reaction. Also, due to the large entrance channel Coulomb repulsion (i.e., $Z_P Z_T = 1184$), the nCN content is expected to contribute towards the total capture cross sections.

Therefore, after attaining insight into the fusion-fission dynamics and fission anisotropies, we next intend to study the contribution of competing nCN decay channels in the decay of the $^{216}\text{Th}^*$ nucleus. As per the experimental observations of Zhang *et al.* [19], the capture cross sections ($\sigma_{capt.}$) include the contributions from CN and nCN processes, i.e., $\sigma_{capt.} = \sigma_{CN} + \sigma_{nCN}$. The pure compound nucleus formation cross sections (σ_{CN}) include only evaporation residue (ER) and fusion-fission (ff) cross sections: $\sigma_{CN} = \sigma_{ER} + \sigma_{ff}$. On the other hand, the hindrance in the formation of CN can be addressed in terms of nCN cross sections (σ_{nCN}) which involve contributions from quasifission (QF) and fast fission (FF) processes, i.e., $\sigma_{nCN} = \sigma_{QF} + \sigma_{FF}$. The ΔR values for ff, QF, and FF are optimized in reference to [19], where the relative contribution of different fission mechanisms is explored. It is worth mentioning that the cross sections are calculated using partial wave analysis as described in Eqs. (1) and (2). In the case of quasifission (QF), the projectile is captured by the target nucleus, and a nonequilibrated composite system (called a dinuclear system) is formed, which is trapped in the potential well for a very short time. In this case, multinucleon transfer takes place, and the formed composite system reseparates at a faster pace (as compared to equilibrated CN), and hence projectile-like fragments appear in the exit channel, and QF is observed. In DCM based calculations, the QF contributions are calculated by considering preformation probability equal to unity ($P_0 = 1$) for the incoming channel [45], since for the QF process the target and projectile nuclei are supposed to retain their identity [54,55]. The penetration probability (P_{ic}) is calculated for the decay fragments, which are identical to the incoming channel, using the WKB approximation, and then the QF cross section reads as

$$\sigma_{QF} = \frac{\pi}{k^2} \sum_{\ell=0}^{\ell_{max}} (2\ell + 1) P_{ic}. \quad (14)$$

TABLE II. The DCM-calculated fusion-fission σ_{ff} , quasifission σ_{QF} , and fast fission σ_{FF} cross sections for $^{216}\text{Th}^*$ nucleus at center-of-mass energies ranging from 118.8 to 195.9 MeV. The predicted evaporation residue (ER) contributions using $\Delta R_{\text{ER}} = \Delta R_{\text{ff}} + 0.5$ fm are also presented. The total sum of all evaporation and fission excitation functions (i.e., $\sigma_{\text{capt.}} = \sigma_{\text{ER}} + \sigma_{\text{ff}} + \sigma_{\text{QF}} + \sigma_{\text{FF}}$) compared with the experimental data [19]. Also tabulated are the relevant fitted neck-length parameters ΔR , temperatures T , and excitation energies E_{CN}^* .

$E_{\text{c.m.}}$ (MeV)	E_{CN}^* (MeV)	T (MeV)	ℓ_{max} (\hbar)	ΔR_{ER} (fm)	σ_{ER} (mb)	ΔR_{ff} (fm)	σ_{ff} (mb)	ΔR_{QF} (fm)	σ_{QF} (mb)	ΔR_{FF} (fm)	σ_{FF} (mb)	$\sigma_{\text{capt.}}^{\text{DCM}}$ (mb)	$\sigma_{\text{capt.}}^{\text{Expt.}}$ (mb)
118.8	37.2	1.266	125	1.169	0.00173	0.669	0.0096	0.300	0.0263	0.529	0.0024	0.04	0.04
123.1	41.5	1.336	125	1.250	0.0951	0.750	0.886	0.625	1.45	0.545	0.007	2.44	2.35
127.3	45.8	1.402	125	1.392	0.0852	0.892	16.08	0.848	12.7	0.549	0.012	28.87	22.97
131.5	50.0	1.464	125	1.490	0.974	0.990	47.0	0.918	28.8	0.566	0.0306	76.80	81.01
135.8	54.3	1.525	125	1.554	1.48	1.054	82.6	0.960	42.9	0.577	0.064	127.04	132.27
141.1	58.5	1.582	126	1.584	2.20	1.084	109.4	0.990	58.3	0.628	0.756	170.66	189.33
144.4	61.8	1.626	126	1.625	3.87	1.125	141.0	1.020	75.5	0.668	2.44	222.81	237.06
157.6	76.0	1.800	129	1.675	7.53	1.175	264.0	1.090	150.0	0.750	52.8	474.33	580.0
183.2	101.0	2.072	136	1.680	10.7	1.180	292.0	1.210	460.0	0.845	154.4	917.10	985.0
195.9	114.0	2.200	139	1.685	17.2	1.185	300.0	1.240	581.0	0.846	216.0	1114.2	1110.0

Further, in the case of fast fission (FF) process, a mononucleus is formed that survived QF. The angular momentum of the mononucleus is very large. The fission barrier (B_{f}) of this rotating system disappears at large value of angular momentum due to higher rotational energy [9]. Thus, a hot and rotating nucleus undergoes fast fission, and leads to the formation of two fission fragments similar to those in the fusion-fission (ff) process. Note that fast fission products have properties like those of usual fusion-fission fragments [1]. For the case of fast fission the preformation probability P_0 is calculated by solving the Schrödinger equation shown in Eq. (5) for fission fragments ($A_2 = 72\text{--}99$ plus complementary fragments), for angular momentum values varying from ℓ_{Bf} to ℓ_{max} (where ℓ_{Bf} is an angular momentum at which the fission barrier disappears). Here barrier penetration probability is considered to be maximum (i.e., $P = 1$), in agreement with Ref. [56]. For the reaction under study, ℓ_{Bf} is $70\hbar$ as per the results obtained by Ref. [49] using the finite range model. Thus, the fast fission contributions are calculated using the following formula:

$$\sigma_{\text{FF}} = \frac{\pi}{k^2} \sum_{\ell_{\text{Bf}}}^{\ell_{\text{max}}} (2\ell + 1) P_0. \quad (15)$$

Table II represents the DCM calculated cross sections along with corresponding values of neck-length parameters ΔR , temperatures T , excitation energies E_{CN}^* , and center-of-mass energies $E_{\text{c.m.}}$ for the decay of the $^{216}\text{Th}^*$ nucleus for ER, ff, QF, and FF processes.

The ER cross sections (σ_{ER}) are predicted by using $\Delta R_{\text{ER}} = \Delta R_{\text{ff}} + 0.5$ fm. It is relevant to mention that lighter fragments are generally emitted first from the hot and rotating nuclei, establishing the fact that light particle emission occurs prior to the fission process. Keeping this in mind, higher ΔR is taken for ER formation as compared to the fission decay [27]. The estimated σ_{ER} are found to be negligibly small, in agreement with the experimental observations [19]. DCM based cross-sections of ER, ff, QF, and FF processes, i.e., $\sigma_{\text{capt.}}^{\text{DCM}}$, show nice agreement with experimental measured [19] capture data ($\sigma_{\text{capt.}}^{\text{Expt.}}$) at all energies.

Next, to explore the quasifission (QF) process, the interaction potential $V(R, \ell)$ is plotted in Fig. 3(a) for the $^{32}\text{S} + ^{184}\text{W}$ reaction at $E_{\text{c.m.}} = 195.9$ MeV, for the minimum ($\ell = 0$) and maximum ($\ell_{\text{max}} = 139\hbar$) angular momentum values. QF is a process in which a nonequilibrated composite system disintegrates into two fragments without reaching the equilibrated shape of the compound nucleus (CN). According to the DNS model [19], the depth of the potential well is called the quasifission barrier (B_{QF}), as marked in the figure. It is depicted in the figure that the interaction potential changes due to the increase in the rotational energy V_{ℓ} , and the depth of the potential well decreases with increase in ℓ . That means the value of B_{QF} decreases; in contrast the Coulomb barrier $B_{\text{Coul.}}$ increases with increase in ℓ . Similar results can be observed in Fig. 3(b) plotted for B_{QF} and $B_{\text{Coul.}}$ as a function of ℓ . Clearly, it indicates that at higher ℓ values the higher Coulomb barrier and lower QF barrier reduce the possibility of formation of an

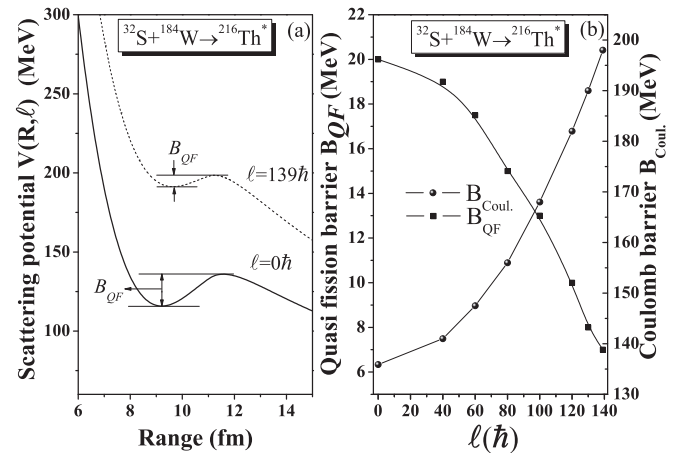


FIG. 3. (a) Variation of interaction potential [$V(R) = V_p + V_c + V_{\ell}$] as a function of range R (fm) for quasifission at $E_{\text{c.m.}} = 195.9$ MeV for ℓ_{min} and ℓ_{max} values. (b) Quasifission barrier (B_{QF}) and Coulomb barrier ($B_{\text{Coul.}}$) as a function of angular momentum ℓ (\hbar) at $E_{\text{c.m.}} = 195.9$ MeV.

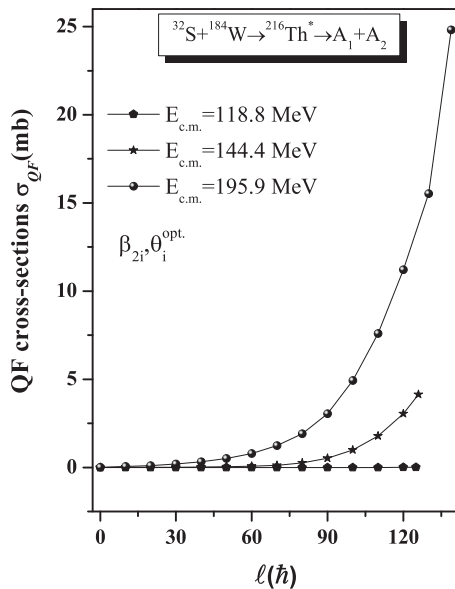


FIG. 4. (a) Quasifission cross sections σ_{QF} as a function of angular momentum $\ell(\hbar)$ for the $^{216}\text{Th}^*$ nucleus at three center-of-mass energies, $E_{\text{c.m.}} = 118.8, 144.4,$ and 195.9 MeV.

equilibrated CN state, and hence the contribution of the QF process increases at higher ℓ values.

The QF cross sections (σ_{QF}) are plotted as a function of ℓ , for three center-of-mass energies, in Fig. 4. At lowest $E_{\text{c.m.}} = 118.8$ MeV, the variation in QF cross section at a given ℓ value is not very significant as compared to two higher energies $E_{\text{c.m.}} = 144.4$ and 195.9 MeV. The QF contribution is quite small at smaller angular momentum values (up to $\ell = 50\hbar$), but for $\ell > 50\hbar$, σ_{QF} increases as a function of angular momentum. These results further support the observation that higher excitation energies and higher angular mo-

mentum show the maximum contribution of the quasifission mechanism.

After studying the variation of angular momentum and collision energy for the QF mechanism, Fig. 5 shows the ℓ -summed preformation probability P_0 and cross section σ as a function of contributing fragments (A_2) of fusion-fission (ff) and fast fission (FF) processes of the $^{216}\text{Th}^*$ nucleus at two extreme energies $E_{\text{c.m.}} = 118.8$ MeV and 195.9 MeV. The ff is analyzed for partial waves $\ell = 0$ to $\ell = \ell_{\text{max}}$, and the FF process contributes in the $\ell_{\text{Bf}} \leq \ell \leq \ell_{\text{max}}$ window. It is clearly evident from the figure that the preformation probability for both processes follows similar trend, exhibiting significantly large magnitude for the ff process. At highest $E_{\text{c.m.}}$ the probability of preformed FF fragments starts competing with the preformation probability of ff fragments. Similar results can be seen from panel (b) of Fig. 5: σ_{ff} is larger in magnitude than σ_{FF} at lowest energy; however, they compete with each other at highest energy. From Figs. 4 and 5 one may conclude that the nCN fission components have more prominent contribution at higher ℓ values and higher energies. This observation is in agreement with the conclusion extracted from the anomalous behavior of fission anisotropies A (see Table I) that the above-barrier energies contribute most towards the nCN content.

A comparative study of DCM calculated cross sections of fusion-fission, quasifission, and fast fission processes as a function of $E_{\text{c.m.}}$ is presented in Fig. 6. The predicted ER cross sections (σ_{ER}) are not shown in this figure as they have negligible values (see Table II). Clearly, one can see from the figure that the contribution of both CN and nCN processes is large at higher energies. The fusion-fission is major contributor to the capture cross-sections in the energy range $127.3 < E_{\text{c.m.}} < 157.6$ MeV. Above 157.6 MeV the multinucleon transfer processes such as quasifission have larger contribution than fusion-fission, which means that CN formation is hindered at higher energies. The contribution from another nCN process, i.e., fast fission, is relatively small as compared to other decay

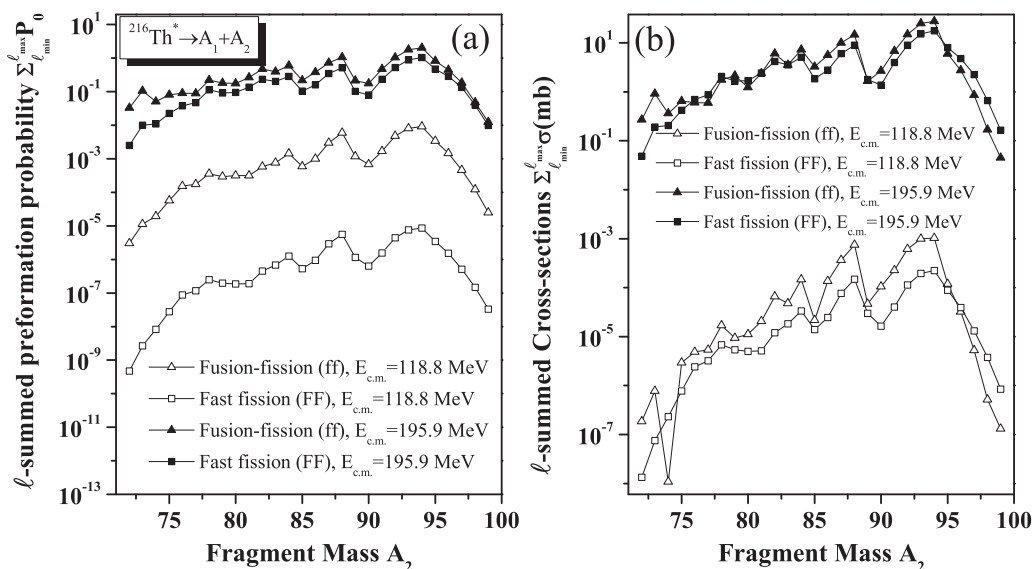


FIG. 5. (a) ℓ -summed preformation probability P_0 plotted for fusion-fission and fast fission decay of the $^{216}\text{Th}^*$ nucleus at two extreme $E_{\text{c.m.}}$ as a function of fragment mass A_2 . Panel (b) represents the same but for ℓ -summed fusion-fission (σ_{ff}) and fast fission (σ_{FF}) cross sections.

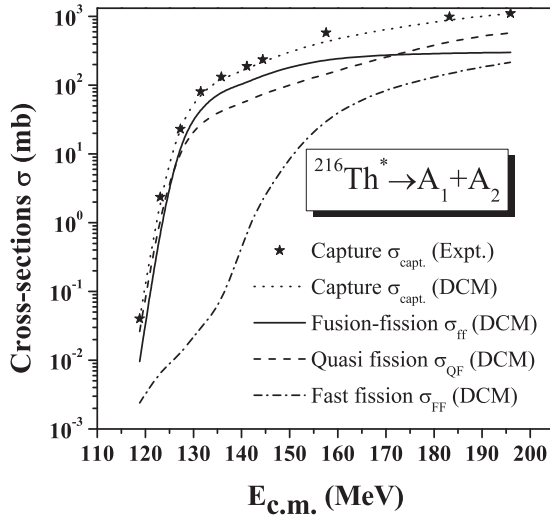


FIG. 6. Individual contribution of different fission channels as a function of center-of-mass energy $E_{c.m.}$ and comparison of DCM calculated capture cross sections with experimental [19] capture data for the $^{32}\text{S} + ^{184}\text{W} \rightarrow ^{216}\text{Th}^*$ reaction.

processes, but starts competing with the fusion-fission process at very highest energies. DCM calculations were done to identify the individual contributions of the contributing decay processes. Also, it is worth mentioning that the sum of all three fission excitation functions (i.e., $\sigma_{\text{capt.}}^{\text{DCM}}$) is in agreement with the experimental [19] capture cross section ($\sigma_{\text{capt.}}^{\text{Expt.}}$) at all collision energies $E_{c.m.}$.

The above results clearly indicate that, at higher energies and ℓ values, the nCN process starts competing with the fusion-fission process. In view of this, the compound nucleus fusion/formation probability (P_{CN}) is calculated for the $^{216}\text{Th}^*$ nucleus within the framework of DCM as a function of $E_{c.m.}$. The CN fusion probability P_{CN} is a parameter which describes the probability of complete fusion. If $P_{\text{CN}} \approx 1$, it is assumed that there is complete formation of a compound nucleus, otherwise the presence of other nCN decays is anticipated. The P_{CN} is calculated using [57]

$$P_{\text{CN}} = \frac{\sigma_{\text{CN}}}{\sigma_{\text{CN}} + \sigma_{\text{nCN}}} = \frac{\sigma_{\text{ER}} + \sigma_{\text{ff}}}{\sigma_{\text{ER}} + \sigma_{\text{ff}} + \sigma_{\text{QF}} + \sigma_{\text{FF}}}. \quad (16)$$

Figure 7 depicts the variation of DCM-calculated P_{CN} as a function of center-of-mass energy $E_{c.m.}$ for the $^{216}\text{Th}^*$ nucleus, and compares with the ones obtained by the dinuclear system (DNS) model [19]. The figure clearly shows the strong hindrance to the fusion/formation of the CN at lower and higher center-of-mass energies. It is seen from figure that the CN fusion factor first increases with energy up to ≈ 136 MeV (around Coulomb barrier energy), and then shows decreasing behavior as a function of $E_{c.m.}$. Initially, the projectile has not enough energy to overcome the Coulomb barrier and fuse with the target, hence P_{CN} has smaller values at lower $E_{c.m.}$. On the other hand, at above-barrier energies, the lowering of the P_{CN} factor is connected with the large contribution of nCN fission, i.e., quasifission and fast fission. Also, $P_{\text{CN}} > 0.5$ for the $^{216}\text{Th}^*$ nucleus in the energy range $127.3 < E_{c.m.} <$

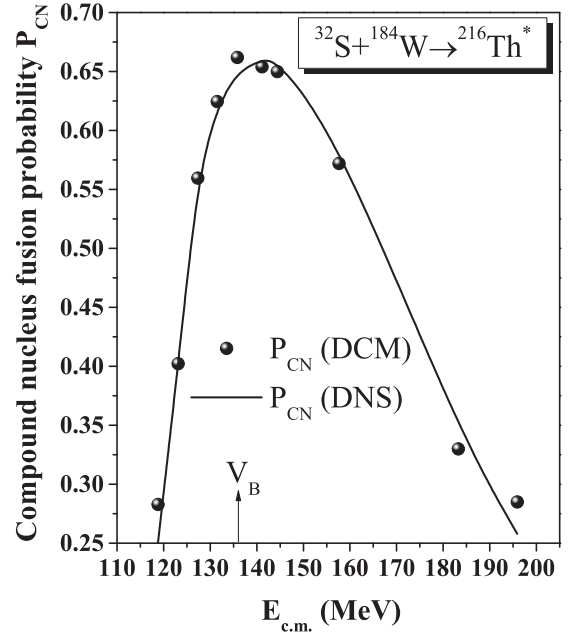


FIG. 7. DCM calculated compound nucleus fusion/formation probability P_{CN} as a function of center-of-mass energy $E_{c.m.}$ for the $^{32}\text{S} + ^{184}\text{W} \rightarrow ^{216}\text{Th}^*$ reaction, and comparison with the DNS calculated P_{CN} .

157.6 MeV due to the large fusion-fission cross sections as compared to the nCN cross sections, also shown in Fig. 6. The largest value of P_{CN} for the studied reaction is 0.66.

B. Role of “dynamic deformations” on the various decay mechanisms of the $^{216}\text{Th}^*$ nucleus

In this section, the specific role of temperature-dependent deformations of decaying fragments is investigated by comparing the results with the static choice of deformations. Figure 8 shows the fragmentation potential $V(A_2)$ for the $^{216}\text{Th}^*$ nucleus at highest $E_{c.m.} = 195.9$ MeV ($T = 2.2$ MeV), plotted for β_2 -static and β_2 -dynamic choices of deformation. Note that at highest $E_{c.m.} = 195.9$ MeV, the nCN fission mechanisms compete with the CN processes, as depicted in Sec. III A, hence the effect of β_2 -dynamic deformations is analyzed at highest energy. It is evident from the figure that the decay structure of the fragmentation potential is significantly modified when β_2 -static deformations are replaced with β_2 -dynamic deformations. Asymmetric fission forms the dominant decay mode for the choice of β_2 -static deformations, as discussed in the previous section. After the inclusion of T -dependent deformations, the symmetric fission starts competing with the asymmetric component. The DCM calculations suggest that symmetric fission contributes $\approx 31\%$ towards the total fusion-fission cross section of the $^{216}\text{Th}^*$ nucleus for β_2 -dynamic choice at $E_{c.m.} = 195.9$ MeV. Independently of the type of deformation, the choice of most preferred decay fragments in asymmetric fission remains identical. It may be noted that at higher temperature (e.g., $T = 2.2$ MeV), the characteristic behavior of the fragmentation potential is similar for spherical and dynamical choices of deformation (not

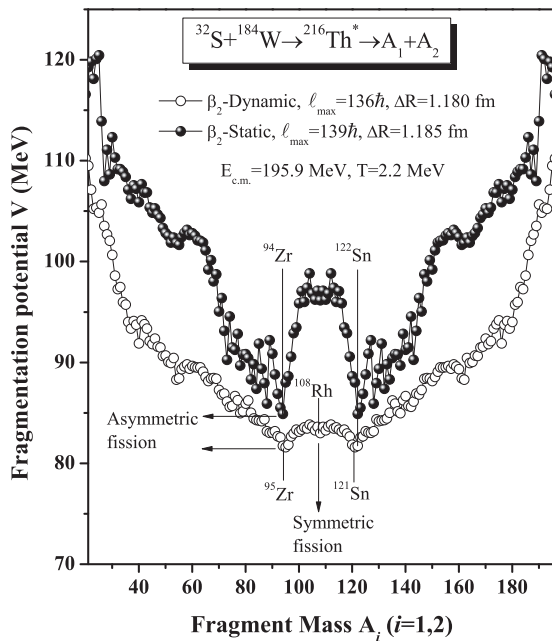


FIG. 8. Fragmentation potential $V(A_i)$ for the $^{216}\text{Th}^*$ nucleus plotted at $E_{c.m.} = 195.9$ MeV and $T = 2.2$ MeV for β_2 -static and β_2 -dynamic deformations of fragments.

shown here). Broadly speaking, for the case of β_2 dynamic, the mass distribution gets broader, and more decay fragments start contributing to the fission process including asymmetric ($A_2 = 72-99$) and symmetric ($A_2 = 100-108$) fission fragments.

For further analysis, the interaction potential $V(R)$ is calculated for the $^{32}\text{S} + ^{184}\text{W}$ reaction using β_2 -static and β_2 -

dynamic choices of deformation as shown in Fig. 9(a) at $E_{c.m.} = 195.9$ MeV. It is observed that the use of dynamic deformations influence the barrier characteristics (barrier position and barrier height), which in turn affects the tunneling probability and hence the cross sections. For the case of β_2 -dynamic deformations the interaction radius is higher and the interaction barrier is lower as compared to the β_2 -static case. It may be noted that the minute change in the distance between the two interacting nuclei affects the equilibrium between attractive (V_P) and repulsive (V_C and V_l) forces. Following this description, the quasifission barrier (B_{QF}) is extracted from the scattering plot [Fig. 9(a)] for the β_2 -dynamic deformations and compared with the β_2 -static case. As the interaction radius is large for the dynamic deformations in comparison with the static one, the V_P , V_C , and V_l potentials get influenced due to their dependence on R . Hence the overall interaction potential (barrier pocket and barrier height) gets modified after the inclusion of β_2 -dynamic deformations. Therefore, the magnitude of B_{QF} is different for the two choices of deformation, i.e., relatively higher magnitude is observed for the β_2 -static case, as depicted in the inset of Fig. 9(a). As a consequence, the QF cross sections are affected by the choice of deformation as shown in Fig. 9(b). The QF cross sections increase with increase in ℓ value independently of the choice of deformation, where the magnitude of σ_{QF} is larger for the β_2 -dynamic case as compared to the β_2 -static deformations.

Finally, to explore the relative role of static and dynamic deformations on the fast fission (FF) process, the ℓ -summed preformation probability $P_0(A_2)$ and cross sections $\sigma(A_2)$, with summation up to ℓ_{max} , are plotted in Fig. 10 at $E_{c.m.} = 195.9$ MeV. Note that the FF process contributes only for the $\ell_{BF} \leq \ell \leq \ell_{max}$ window where fission barrier vanishes. Figure 10 depicts that σ follows the behavior of P_0 , which

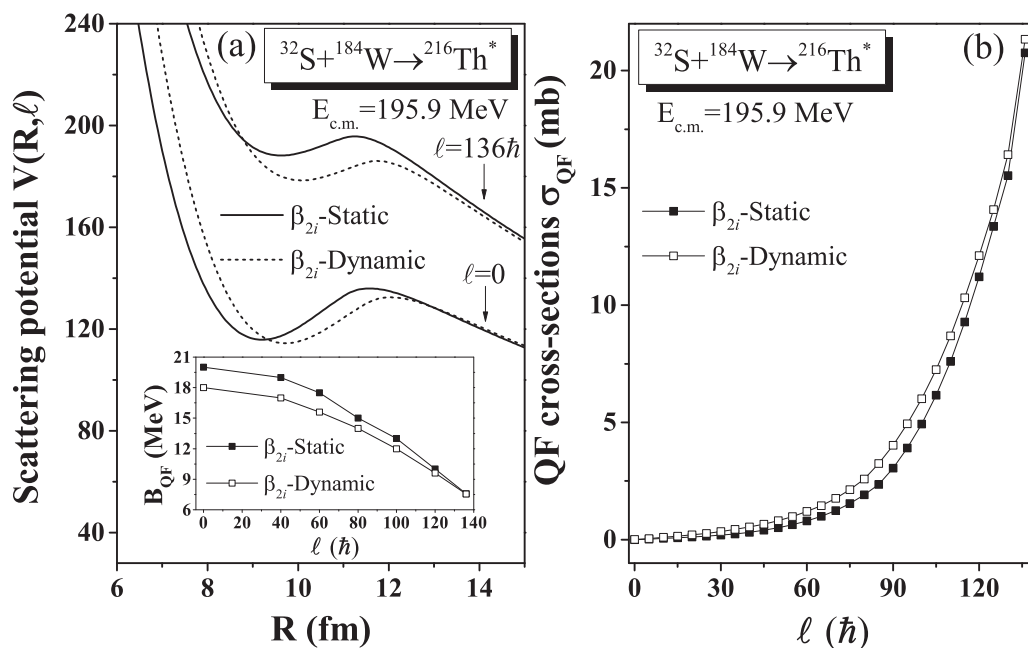


FIG. 9. (a) DCM calculated scattering potential $V(R)$ plotted for the $^{32}\text{S} + ^{184}\text{W}$ reaction at $E_{c.m.} = 195.9$ MeV for both β_2 -static and β_2 -dynamic deformations; the inset of the figure shows the comparison of quasifission barrier B_{QF} for both types of deformation. (b) Calculated quasifission cross sections σ_{QF} plotted for the $^{32}\text{S} + ^{184}\text{W}$ reaction for both choices of deformation.

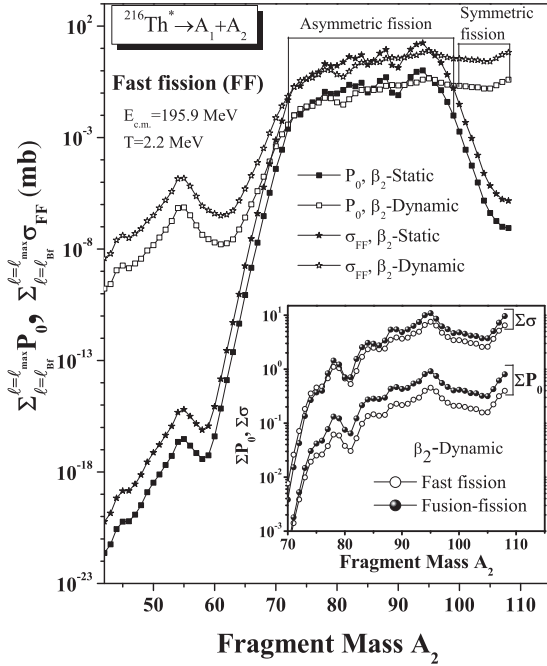


FIG. 10. (a) The ℓ -summed preformation probability P_0 and cross section σ for the FF process of $^{216}\text{Th}^*$ as a function of fragment mass A_2 for both β_2 -static and β_2 -dynamic deformations at $E_{c.m.} = 195.9$ MeV. The inset of the figure represents the variation of ℓ -summed P_0 and σ for both FF and ff mechanisms for the β_2 -dynamic case.

shows an interesting structure with significant contribution of preformation factor for fission fragments. The behavior of preformation probability P_0 gets modified after the inclusion of dynamic deformations. The fragment mass distribution starts broadening and symmetric fission fragments contribute towards the total fission of the $^{216}\text{Th}^*$ nucleus. These results overlay with the information extracted from Fig. 8 for the fusion-fission process. Besides this, the variation of ℓ -summed P_0 and σ (see inset of Fig. 10) for both ff and FF processes shows that the contribution of fast fission competes with the ff component in agreement with the β_2 -static case at the considered energy. An explicit representation of cross sections for ff, QF, and FF processes is given in Table III.

It will be of further interest to extend this work to other nuclear reactions with different entrance channels (e.g., $^{12}\text{C} +$

TABLE III. The DCM-calculated fission cross sections using β_2 -dynamic deformations of fragments for the decay of the $^{216}\text{Th}^*$ nucleus at $E_{c.m.} = 195.9$ MeV ($T = 2.2$ MeV).

ΔR	ℓ_{\max}	σ
1.180 fm	Fusion-fission (ff)	302 mb
	136 \hbar	
1.257 fm	Quasifission (QF)	584 mb
	136 \hbar	
0.550 fm	Fast fission (FF)	232 mb

^{204}Po and $^{40}\text{Ar} + ^{176}\text{Hf}$) forming the same CN (i.e., $^{216}\text{Th}^*$). As discussed in the Introduction, the entrance channel properties play an important role in the dynamics associated with CN and nCN channels. According to Bohr's hypothesis [58], the considered reactions should give the same fusion cross sections. But, in reactions prone to the nCN channel, the probability of complete (pure) fusion is reduced considerably and this results in suppression of fusion cross sections. This suppression of measured fusion cross section is treated as evidence of nCN fission. Further, if the inhibition is caused by the presence of nCN fission, one may also find its evidence in terms of fission mass distributions, because nCN fission has a broader mass distribution than CN fission [59]. Relevant experimental analysis is called for, as it can provide insight regarding decay patterns of the Th nucleus.

IV. SUMMARY

Different competing decay mechanisms (ER, ff, QF, FF) emerging via CN and nCN processes of the $^{32}\text{S} + ^{184}\text{W} \rightarrow ^{216}\text{Th}^*$ reaction are studied within the framework of DCM. The analysis is carried out over a wide range of collision energies varying from $E_{c.m.} = 118.8$ to 195.9 MeV for β_2 -static deformed choice of fragmentation using optimum orientations. At above-barrier energies, the measured fission anisotropies are anomalous with regard to the SSPSM calculated anisotropies, indicating the presence of nCN content. For the decay of the $^{216}\text{Th}^*$ nucleus, the fission structure shows an asymmetric pattern independent of center-of-mass energy. The capture cross sections are calculated by adding CN ($\sigma_{\text{ER}} + \sigma_{\text{ff}}$) and nCN ($\sigma_{\text{QF}} + \sigma_{\text{FF}}$) contributions, which show nice agreement with the experimental data. As expected, the predicted σ_{ER} are small at all collision energies.

The small QF barrier at higher ℓ values indicates the large contribution of the quasifission mechanism. Consequently, the possibility of compound nucleus formation decreases at higher ℓ values. The fast fission component is analyzed in a higher ℓ window ($\ell_{\text{Bf}} \leq \ell \leq \ell_{\text{max}}$), where the fission barrier disappears. In addition to ℓ dependence, the CN and nCN contributions also show energy dependence. The contribution of QF and FF increases with increase in energy and starts competing with the ff process at above-barrier energies. The calculated compound nucleus fusion/formation probability P_{CN} depicts strong hindrance to the CN formation at lower and higher energies. The small value of P_{CN} at higher $E_{c.m.}$ is connected with large nCN contributions. At lower $E_{c.m.}$ values, the projectile may not have enough energy to overcome the Coulomb barrier and fuse with the target, thereby the probability of CN formation is reduced. The maximum value of P_{CN} is 0.66 near the Coulomb barrier. Finally, the role of dynamic deformations on CN and nCN decay of the $^{216}\text{Th}^*$ nucleus is explored at highest energy. The study reveals that both symmetric and asymmetric fission components start contributing towards the total fission cross sections after the inclusion of dynamic deformations, whereas asymmetric fission is the prime contributor for the β_2 -static case. The barrier characteristics are different for static and dynamic deformations, and accordingly affect the contribution of various decay mechanisms involved in the dynamics of the $^{32}\text{S} + ^{184}\text{W}$ reaction.

ACKNOWLEDGMENTS

Financial support from the Department of Science and Technology (DST), Government of India, under Grant No. EMR/2016/000008, and from the University Grants Com-

mission (UGC), in the form of a Maulana Azad National Fellowship (MANF), is gratefully acknowledged. Further, the authors gratefully acknowledge Dr. Gurvinder Kaur for fruitful discussions related to this work.

-
- [1] A. K. Nasirov, K. Kim, G. Mandaglio, G. Giardina, A. Muminov, and Y. Kim, *Eur. Phys. J. A* **49**, 147 (2013).
- [2] A. K. Nasirov, G. Giardina, G. Mandaglio, M. Manganaro, F. Hanappe, S. Heinz, S. Hofmann, A. I. Muminov, and W. Scheid, *Phys. Rev. C* **79**, 024606 (2009).
- [3] G. Fazio, G. Giardina, G. Mandaglio, F. Hanappe, A. I. Muminov, A. K. Nasirov, W. Scheid, and L. Stuttge, *Mod. Phys. Lett. A* **20**, 391 (2005).
- [4] K. Banerjee, T. K. Ghosh, P. Roy, S. Bhattacharya, A. Chaudhuri, C. Bhattacharya, R. Pandey, S. Kundu, G. Mukherjee, T. K. Rana, J. K. Meena, G. Mohanto, R. Dubey, N. Saneesh, P. Sugathan, R. Guin, S. Das, and P. Bhattacharya, *Phys. Rev. C* **93**, 064602 (2016).
- [5] V. I. Zagrebaev and W. Greiner, *Nucl. Phys. A* **944**, 257 (2015).
- [6] U. L. Businaro and S. Gallone, *Nuovo Cimento* **5**, 315 (1957); K. T. Davies and A. J. Sierk, *Phys. Rev. C* **31**, 915 (1985).
- [7] D. J. Hinde, M. Dasgupta, J. R. Leigh, J. P. Lestone, J. C. Mein, C. R. Morton, J. O. Newton, and H. Timmers, *Phys. Rev. Lett.* **74**, 1295 (1995).
- [8] C. Gregoire, C. Ngo, E. Tomasi, B. Remaud, and F. Scheuter, *Nucl. Phys. A* **387**, 37c (1982).
- [9] B. Borderie, M. Berlinger, D. Gardes, F. Hanappe, L. Nowicki, J. Peter, B. Tamain, S. Agarwal, J. Girard, C. Gregoire, J. Matuszek, and C. Ngo, *Z. Phys. A* **299**, 263 (1981).
- [10] C. Ngo, C. Gregoire, B. Remaud, and E. Tomasi, *Nucl. Phys. A* **400**, 259c (1983).
- [11] B. B. Back, *J. Phys.: Conf. Ser.* **282**, 012003 (2011).
- [12] V. S. Ramamurthy and S. S. Kapoor, *Phys. Rev. Lett.* **54**, 178 (1985).
- [13] S. Kailas, *Phys. Rep.* **284**, 381 (1997).
- [14] G. Kaur and M. K. Sharma, *Int. J. Mod. Phys. E* **23**, 1450063 (2014).
- [15] S. Bhattacharya *et al.*, *EPJ Web Conf.* **86**, 00004 (2015).
- [16] A. Pulcini *et al.*, *J. Phys.: Conf. Ser.* **1014**, 012013 (2018).
- [17] V. S. Ramamurthy, S. S. Kapoor, R. K. Choudhury, A. Saxena, D. M. Nadkarni, A. K. Mohanty, B. K. Nayak, S. V. Sastry, S. Kailas, A. Chatterjee, P. Singh, and A. Navin, *Phys. Rev. Lett.* **65**, 25 (1990).
- [18] R. Rafiei, R. G. Thomas, D. J. Hinde, M. Dasgupta, C. R. Morton, L. R. Gasques, M. L. Brown, and M. D. Rodriguez, *Phys. Rev. C* **77**, 024606 (2008).
- [19] H. Q. Zhang, C. L. Zhang, C. J. Lin, Z. H. Liu, F. Yang, A. K. Nasirov, G. Mandaglio, M. Manganaro, and G. Giardina, *Phys. Rev. C* **81**, 034611 (2010).
- [20] N. Grover, G. Kaur, and M. K. Sharma, *Phys. Rev. C* **93**, 014603 (2016).
- [21] G. Kaur, K. Sandhu, and M. K. Sharma, *Phys. Rev. C* **94**, 014615 (2016).
- [22] A. Kaur, G. Kaur, and M. K. Sharma, *Nucl. Phys. A* **941**, 152 (2015).
- [23] G. Sawhney, A. Kaur, M. K. Sharma, and R. K. Gupta, *Phys. Rev. C* **92**, 064303 (2015).
- [24] G. Kaur and M. K. Sharma, *Phys. Rev. C* **87**, 044601 (2013); *Nucl. Phys. A* **884**, 36 (2012).
- [25] G. Sawhney, G. Kaur, M. K. Sharma, and R. K. Gupta, *Phys. Rev. C* **88**, 034603 (2013).
- [26] Rajni, R. Kumar, and M. K. Sharma, *Phys. Rev. C* **90**, 044604 (2014).
- [27] M. Kaur and M. K. Sharma, *Eur. Phys. J. A* **50**, 61 (2014).
- [28] R. Vandenbosch and J. R. Huizenga, *Nuclear Fission* (Academic, New York, 1973).
- [29] M. Muenchow and W. Scheid, *Phys. Lett. B* **162**, 265 (1985); *Nucl. Phys. A* **468**, 59 (1987).
- [30] M. Rashdan, A. Faessler, and W. Waida, *J. Phys. G: Nucl. Part. Phys.* **17**, 1401 (1991).
- [31] A. Kaur and M. K. Sharma, *AIP Conf. Proc.* **2006**, 030001 (2018).
- [32] H. J. Fink, J. Maruhn, W. Scheid, and W. Greiner, *Z. Phys.* **268**, 321 (1974).
- [33] J. Maruhn and W. Greiner, *Phys. Rev. Lett.* **32**, 548 (1974).
- [34] R. K. Gupta, W. Scheid, and W. Greiner, *Phys. Rev. Lett.* **35**, 353 (1975).
- [35] B. B. Singh, M. K. Sharma, and R. K. Gupta, *Phys. Rev. C* **77**, 054613 (2008).
- [36] N. J. Davidson, S.S. Hsiao, J. Markram, H. G. Miller, and Y. Tzeng, *Nucl. Phys. A* **570**, 61c (1994).
- [37] W. D. Myers and W. J. Swiatecki, *Nucl. Phys.* **81**, 1 (1966).
- [38] A. S. Jensen and J. Damgaard, *Nucl. Phys. A* **203**, 578 (1973).
- [39] R. K. Gupta, R. Kumar, N. K. Dhiman, M. Balasubramaniam, W. Scheid, and C. Beck, *Phys. Rev. C* **68**, 014610 (2003).
- [40] M. Balasubramaniam, R. Kumar, R. K. Gupta, C. Beck, and W. Scheid, *J. Phys. G: Nucl. Part. Phys.* **29**, 2703 (2003).
- [41] G. Audi, A. H. Wapstra, and C. Thibault, *Nucl. Phys. A* **729**, 337 (2003).
- [42] P. Möller, J. R. Nix, W. D. Myers, and W. J. Swiatecki, *At. Data Nucl. Data Tables* **59**, 185 (1995).
- [43] R. K. Gupta, M. Balasubramaniam, R. Kumar, N. Singh, M. Manhas, and W. Greiner, *J. Phys. G: Nucl. Part. Phys.* **31**, 631 (2005); R. K. Gupta, M. Manhas, and W. Greiner, *Phys. Rev. C* **73**, 054307 (2006).
- [44] H. Kröger and W. Scheid, *J. Phys. G: Nucl. Part. Phys.* **6**, L85 (1980).
- [45] R. Kumar, M. Bansal, S. K. Arun, and R. K. Gupta, *Phys. Rev. C* **80**, 034618 (2009).
- [46] G. Royer and J. Mignen, *J. Phys. G: Nucl. Part. Phys.* **18**, 1781 (1992).
- [47] G. Sawhney, R. Kumar, and M. K. Sharma, *Phys. Rev. C* **86**, 034613 (2012).
- [48] M. Kaur, M. K. Sharma, and R. K. Gupta, *Phys. Rev. C* **86**, 064610 (2012).
- [49] A. J. Sierk, *Phys. Rev. C* **33**, 2039 (1986).
- [50] A. Kaur, G. Kaur, and M. K. Sharma, *Braz. J. Phys.* **48**, 608 (2018).
- [51] J. Blocki, J. Randrup, W. J. Swiatecki, and C. F. Tsang, *Ann. Phys. (NY)* **105**, 427 (1977).

- [52] C. Wagemans, *The Nuclear Fission Process* (CRC, Boca Raton, FL, 1991).
- [53] R. G. Thomas, R. K. Choudhury, A. K. Mohanty, A. Saxena, and S. S. Kapoor, *Phys. Rev. C* **67**, 041601(R) (2003).
- [54] B. B. Back *et al.*, *Phys. Rev. C* **53**, 1734 (1996); **32**, 195 (1985).
- [55] B. B. Back, *Phys. Rev. C* **31**, 2104 (1985).
- [56] S. S. Kapoor and V. Ramamurthy, *Pramana J. Phys.* **33**, 161 (1989).
- [57] A. Kaur, S. Chopra, and R. K. Gupta, *Phys. Rev. C* **90**, 024619 (2014).
- [58] N. Bohr, *Nature (London)* **137**, 344 (1936).
- [59] A. C. Berriman, D. J. Hinde, M. Dasgupta, C. R. Morton, R. D. Butt, and J. O. Newton, *Nature (London)* **413**, 144 (2001).